ARMA 17-0108

Modeling of tensile and compressive damage in layered sedimentary rock: a direction dependent non-local model

Jin, W. and Arson, C.
Georgia Institute of Technology, Atlanta, GA, USA

ABSTRACT: This paper presents the theoretical formulation and numerical implementation of an anisotropic damage model for materials with intrinsic transverse isotropy, e.g. sedimentary rocks with a bedding plane. The direction dependent mechanical response is captured by utilizing four types of equivalent strains, for tension and compression, parallel and perpendicular to the bedding plane. The model is calibrated against triaxial compression test data, for different confinement and loading orientations. The variations of uniaxial tensile and compressive strengths with the orientation of the loading relative to the bedding follow the trends and magnitudes noted in experiments. Anisotropic non-local equivalent strains were used in the formulation to avoid localization and mesh dependence encountered with strain softening. Two different internal length parameters are used to distinguish the non-local effects along and perpendicular to the bedding. An arc length control algorithm is used to avoid convergence issues. Results of three-point bending tests confirm that the nonlocal approach indeed eliminates mesh dependency. Results show that the orientation and size of the damage process zone are direction dependent, and that materials with intrinsic transverse isotropy exhibit mixed fracture propagation modes except when the bedding aligns with the loading direction. Further research towards a multiscale hydro-mechanical fracture propagation scheme is undergoing.

1. INTRODUCTION

Modeling fracture propagation in sedimentary rocks requires complex coupled constitutive equations to account for both intrinsic and stress-induced anisotropy, and regularized numerical methods to avoid mesh size dependence due to strain softening. Experiments revealed that rock maximum axial compressive strength is reached when weak planes are either parallel or perpendicular to the loading direction, and minimum strength is reached when weak planes are orientated $30° - 60°$ with respect to the loading direction (**Donath, 1961**; **Niandou et al., 1997**; **Pietruszczak and Mroz, 2001**). In indirect tensile tests, the tensile strength is maximum when tensile stress is applied within the weak plane, and gradually decreases as the orientation angle between the tensile stress direction and the bedding plane increases (**Mahjoub et al., 2015**). State-of-the-Art constitutive models are either based on Continuum Damage Mechanics (CDM) or Micromechanics. In CDM, damage criteria and evolution laws for anisotropic materials depend on a second order fabric tensor to account for the direction dependency (**Pietruszczak et al., 2007**). In Micromechanics models, the expression of the free energy is obtained by solving a matrix-inclusion problem for a given set of crack families. Depending on the homogenization scheme, crack interaction may or may not be accounted for. Intrinsic anisotropy is accounted for by attributing different properties to crack families of different orientations (**Chen et al., 2012**). Once implemented in a Finite Element (FE) code, both CDM and micromechanics models suffer from mesh dependence if strain softening is considered for compression/tension. Several localization limiters can be used, e.g. the crack band theory, a non-local integration-based formulation or non-local differentiation-based formulation. However, the non-local effects of intrinsic anisotropy are usually not accounted for.

In this paper, we integrate a measure of strain to formulate a nonlocal anisotropic damage model for sedimentary rock. In Section 2, we present the local damage model, which accounts for the confinement dependence of the compressive behavior, with a compression strength up to one order of magnitude larger than the tension strength. The model allows predicting stress-induced anisotropy in an initially transverse isotropic material. The model is calibrated against stress/strain curves obtained during triaxial compression tests performed on shale. In Section 3, we explain the non-local formulation, which contains two internal lengths to represent intrinsic anisotropy. In Section 4, three point bending simulation results are presented to show that the size of the fracture process zone is direction dependent, but mesh independent. Note that we use Voigt matrix notations throughout the paper. Lower cases are used for scalar variables, bold lower cases for vectors and bold upper cases for matrices.

2. LOCAL ANISOTROPIC DAMAGE MODEL FOR TRANSVERSE ISOTROPIC MATERIALS

2.1. *Constitutive relationship*

In CDM, the effect of damage is taken into account by reducing the values of stiffness. By using strain equivalence principle, the nominal stress, $\hat{\boldsymbol{\sigma}}$, is related to effective stress, $\boldsymbol{\sigma}$, through

$$\boldsymbol{\sigma} = \mathbf{M}\hat{\boldsymbol{\sigma}} \,, \tag{1}$$

Where $\mathbf{M}$ is the damage operator, which has a diagonal form, as follows:

$$M_{ii} = \frac{1}{1-\omega_i}, \;\; i = 1,2,\dots,6 \tag{2}$$

The rock is represented as a transverse isotropic with respect to the direction normal to the bedding plane. We set the local coordinate system so that direction 1 is perpendicular to the bedding plane: ω_1 represents damage variable in axial direction (perpendicular to the bedding), ω_2, ω_3 are damage variables in the transverse directions (along the bedding), the shearing damage variables are expressed as

$$\begin{aligned} \omega_4 &= 1-(1-\omega_2)(1-\omega_3) \\ \omega_5 &= 1-(1-\omega_1)(1-\omega_3) \\ \omega_6 &= 1-(1-\omega_1)(1-\omega_2) \end{aligned} \tag{3}$$

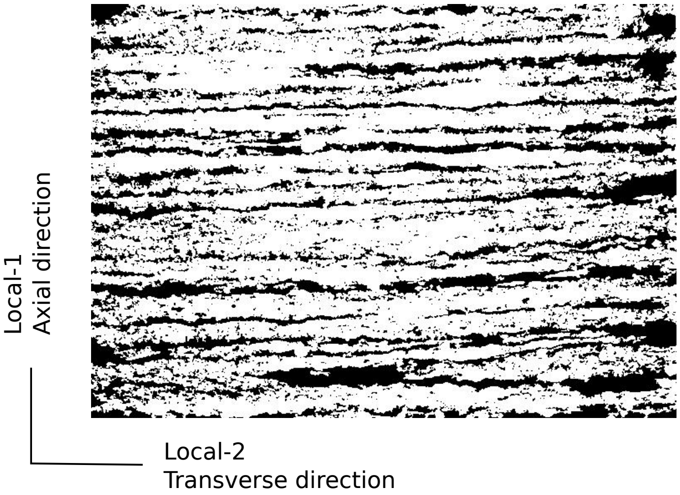

Fig. 1. Definition of the intrinsic damage directions in transverse isotropic shale, modified from (**Bramlette, 1943**).

The transverse isotropic elastic behavior of the material depends on five independent parameters $(E_1, E_2, \nu_{12}, \nu_{23}, G_{12})$. Using the effective stress concept, the compliance matrix can be expressed as:

$$\begin{aligned} \mathrm{S}_{11} &= 1/(1-\omega_1)/E_1 \\ \mathrm{S}_{22} &= 1/(1-\omega_2)/E_2 \\ \mathrm{S}_{33} &= 1/(1-\omega_3)/E_2 \\ \mathrm{S}_{12} &= \mathrm{S}_{13} = -\nu_{12}/\mathrm{E}_2 \\ \mathrm{S}_{21} &= \mathrm{S}_{31} = -\nu_{21}/\mathrm{E}_1 \\ \mathrm{S}_{23} &= \mathrm{S}_{32} = -\nu_{23}/\mathrm{E}_2 \\ \mathrm{S}_{44} &= 2(1+\nu_{23})/(1-\omega_4)/\mathrm{E}_2 \\ \mathrm{S}_{55} &= 1/(1-\omega_5)/\mathrm{G}_{13} \\ \mathrm{S}_{66} &= 1/(1-\omega_6)/\mathrm{G}_{12} \end{aligned} \tag{4}$$

In which we used $\nu_{12}/\mathrm{E}_2 = \nu_{21}/\mathrm{E}_1$ to ensure as symmetry requirements. In order to distinguish tensile and compressive behavior, we distinguish tensile and compressive components of damage in each direction ω_i. We consider that the growth of compressive (respectively tensile) damage does not influence tensile (respectively compressive) damage, which makes it possible to capture unilateral effects. Damage components take values between 0 (no micro-crack in the direction considered) to 1 (no more stiffness in the direction considered).

Two different damage criteria are used to distinguish micro-crack propagation in the axial and transverse directions, as follows:

$$\begin{aligned} g_1(\boldsymbol{\epsilon}, \kappa_1) &= \epsilon_1^{eq} - \kappa_1 \\ g_2(\boldsymbol{\epsilon}, \kappa_2) &= \epsilon_2^{eq} - \kappa_2 \end{aligned} \tag{5}$$

Where the equivalent strains $\epsilon_1^{eq}, \epsilon_2^{eq}$ are scalar measures of strain defined in the axial and transverse directions (detailed below). κ_1, κ_2 serve as internal variables and control the evolution of damage: they represent the largest equivalent strains ever reached during the past loading history of the material. Damage can grow only if the current stress state reaches the boundary of the elastic domain, $g_i = 0$. The consistency conditions are:

$$\begin{aligned} g_1 \le 0, \quad \dot{\kappa_1} \ge 0, \quad \dot{\kappa_1} g_1 = 0 \\ g_2 \le 0, \quad \dot{\kappa_2} \ge 0, \quad \dot{\kappa_2} g_2 = 0 \end{aligned} \tag{6}$$

The equivalent strain will be integrated over a control zone to account for non-local damage effects. Three types of non-local strain variables were used in previous damage models for isotropic materials: the energy release rate thermodynamically conjugated to damage **Antonio and Pijaudier-Cabot, 1994**), the average of the positive principal strain (**Mazars, 1986**), and a modified von Mises strain (**De Vree et al., 1995**). A new equivalent strain measure is needed to account for the direction dependence of transverse isotropic materials. Inspired from Hashin's failure criteria (**Hashin, 1980**) for unidirectional fiber composites, we introduce the following strain invariants with respect to the axial direction:

$$\begin{aligned} I_1 &= \epsilon_{11} \\ I_2 &= \epsilon_{22} + \epsilon_{33} \\ I_3 &= \frac{1}{4}(\epsilon_{22} - \epsilon_{33})^2 + \epsilon_{23}^2 \end{aligned}$$

$$I_4 = \epsilon_{12}^2 + \epsilon_{13}^2$$
$$I_5 = 2\epsilon_{12}\epsilon_{13}\epsilon_{23} - \epsilon_{22}\epsilon_{13}^2 - \epsilon_{33}\epsilon_{12}^2 \quad (7)$$

Following Hill's yield theory (**Hill, 1948**), the most general from of a transversely isotropic quadratic yield criterion is

$$A_1 I_1^2 + A_2 I_2^2 + A_3 I_3 + A_4 I_4 + B_{12} I_1 I_2 = 1 \quad (8)$$

Note: I_5 is omitted because we choose a quadratic yield criterion. If the damage criterion is reached along the axial direction, this is because either the axial strain ϵ_{11} reaches the initial tensile/compressive $\epsilon_{11}^{t0}/\epsilon_{11}^{c0}$ strain threshold, or because the shear strain invariant reaches $(\epsilon_{12}^{s0})^2$. Consequently, we define the equivalent strain for tension and compression as

$$\epsilon_{1t}^{eq} = \sqrt{\epsilon_{11}^2 + (\epsilon_{12}^2 + \epsilon_{13}^2)\left(\frac{\epsilon_{11}^{t0}}{\epsilon_{12}^{s0}}\right)^2}$$
$$\epsilon_{1c}^{eq} = \sqrt{\epsilon_{11}^2 + (\epsilon_{12}^2 + \epsilon_{13}^2)\left(\frac{\epsilon_{11}^{c0}}{\epsilon_{12}^{s0}}\right)^2} \quad (9)$$

Similarly, the equivalent strains in the transverse directions are expressed as

$$\epsilon_{2t}^{eq} = \sqrt{I_2^2 + I_3^2\left(\frac{\epsilon_{22}^{t0}}{\epsilon_{23}^{s0}}\right)^2 + I_4\left(\frac{\epsilon_{22}^{t0}}{\epsilon_{12}^{s0}}\right)^2}$$
$$\epsilon_{2c}^{eq} = \sqrt{I_2^2 + I_3^2\left(\frac{\epsilon_{22}^{c0}}{\epsilon_{23}^{s0}}\right)^2 + I_4\left(\frac{\epsilon_{22}^{c0}}{\epsilon_{12}^{s0}}\right)^2} \quad (10)$$

In which, $\epsilon_{22}^{t0}, \epsilon_{22}^{c0}, \epsilon_{12}^{s0}, \epsilon_{23}^{s0}$ are initial yield strains in tension, compression and shear (the subscripts indicate the directions). To close the constitutive formulation, we link the internal variable κ_i to the damage variable ω_i. Since ω_i and κ_i can only grow monotonically, we postulate the damage evolution law in an explicit form. In materials exhibiting a brittle behavior in tension, damage grows rapidly after the threshold is reached (i.e. micro cracks propagate and coalesce fast). To reflect this phenomenon, we utilize the following exponential function:

$$\omega_{1t} = f(\kappa_1) = 1 - \exp\left(-\frac{\kappa_1 - \epsilon_{11}^{t0}}{\alpha_{11}^t}\right) \quad (11)$$

Where α_{11}^t is a material parameter that controls the growth rate of damage (i.e. the brittleness of material response). Note, damage is considered equal to zero when $\kappa_1 < \epsilon_{11}^{t0}$. Similarly, we express the damage growth function in transverse directions as

$$\lambda_{2t} = f(\kappa_2) = 1 - \exp\left(-\frac{\kappa_2 - \epsilon_{22}^{t0}}{\alpha_{22}^t}\right)$$
$$\omega_{2t} = \frac{2\lambda_{2t}\left\{\epsilon_{22}^2 + \epsilon_{22}\epsilon_{33} + \left[\frac{1}{4}\langle\epsilon_{22} - \epsilon_{33}\rangle^2 + \epsilon_{23}^2\right]\left(\frac{\epsilon_{22}^{t0}}{\epsilon_{23}^{s0}}\right)^2 + \epsilon_{12}^2\left(\frac{\epsilon_{22}^{t0}}{\epsilon_{12}^{s0}}\right)^2\right\}}{\kappa_2^2}$$
$$\omega_{3t} = \frac{2\lambda_{2t}\left\{\epsilon_{33}^2 + \epsilon_{22}\epsilon_{33} + \left[\frac{1}{4}\langle\epsilon_{33} - \epsilon_{22}\rangle^2 + \epsilon_{23}^2\right]\left(\frac{\epsilon_{22}^{t0}}{\epsilon_{23}^{s0}}\right)^2 + \epsilon_{13}^2\left(\frac{\epsilon_{22}^{t0}}{\epsilon_{12}^{s0}}\right)^2\right\}}{\kappa_2^2}$$
$$(12)$$

Where $\langle x \rangle = 0$ if $x < 0$, $\langle x \rangle = x$ if $x \geq 0$. α_{22}^t controls the ductility of the response in the transverse directions.

Unlike in tension, geomaterials in compression exhibit a pressure dependent behavior, transitioning from ductile to brittle as the confining pressure increases. During triaxial compression paths, hardening is often observed before the peak and the post-peak softening. In order to account for this phenomenon, we formulate the global damage evolution function as:

$$\omega_{1c} = f(\kappa_1) = \exp\left(\frac{\kappa_1 - \eta\mathrm{Tr}\boldsymbol{\sigma} - \beta_{11}^c}{\alpha_{11}^c}\right) / \left[1 + \exp\left(\frac{\kappa_1 - \eta\mathrm{Tr}\boldsymbol{\sigma} - \beta_{11}^c}{\alpha_{11}^c}\right)\right] \quad (13)$$

Where η, β_{11}^c and α_{11}^c are parameters that represent the dependence to the confining pressure, the initiation of softening under no confinement and the damage growth rate in axial direction, respectively. Similarly, the compressive damage evolution law can be expressed as

$$\lambda_{2c} = f(\kappa_2) = \exp\left(\frac{\kappa_2 - \eta\mathrm{Tr}\boldsymbol{\sigma} - \beta_{22}^c}{\alpha_{22}^c}\right) / \left[1 + \exp\left(\frac{\kappa_2 - \eta\mathrm{Tr}\boldsymbol{\sigma} - \beta_{22}^c}{\alpha_{22}^c}\right)\right]$$
$$\omega_{2c} = \frac{2\lambda_{2c}\left\{\epsilon_{22}^2 + \epsilon_{22}\epsilon_{33} + \left[\frac{1}{4}\langle\epsilon_{22} - \epsilon_{33}\rangle^2 + \epsilon_{23}^2\right]\left(\frac{\epsilon_{22}^{c0}}{\epsilon_{23}^{s0}}\right)^2 + \epsilon_{12}^2\left(\frac{\epsilon_{22}^{c0}}{\epsilon_{12}^{s0}}\right)^2\right\}}{\kappa_2^2}$$
$$\omega_{3c} = \frac{2\lambda_{2c}\left\{\epsilon_{33}^2 + \epsilon_{22}\epsilon_{33} + \left[\frac{1}{4}\langle\epsilon_{33} - \epsilon_{22}\rangle^2 + \epsilon_{23}^2\right]\left(\frac{\epsilon_{22}^{c0}}{\epsilon_{23}^{s0}}\right)^2 + \epsilon_{13}^2\left(\frac{\epsilon_{22}^{c0}}{\epsilon_{12}^{s0}}\right)^2\right\}}{\kappa_2^2}$$
$$(14)$$

2.2. Calibration of the proposed model

We calibrated the proposed model against experimental stress/strain curves obtained during triaxial compression tests performed on Bakken shale samples. We used ConocoPhillips rock mechanics dataset (**Amendt et al., 2013**). A dedicated MATLAB code employing the Interior Point Algorithm was adopted to minimize the residual between experimental results and numerical predictions.

Figure 2 shows the calibration of the elastic material parameters. Note that only parameters $\mathrm{E}_1, \mathrm{E}_2, \nu_{12}, \nu_{23}$ can be obtained from triaxial compression tests loaded perpendicular (axial) and parallel (transverse) to the bedding plane. In the absence of shearing stress path perpendicular to the bedding, G_{12} cannot be obtained.

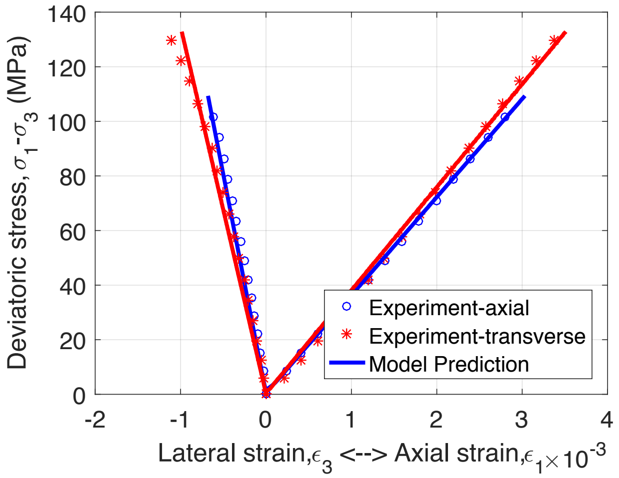

Fig. 2. Calibration of elastic material parameters.

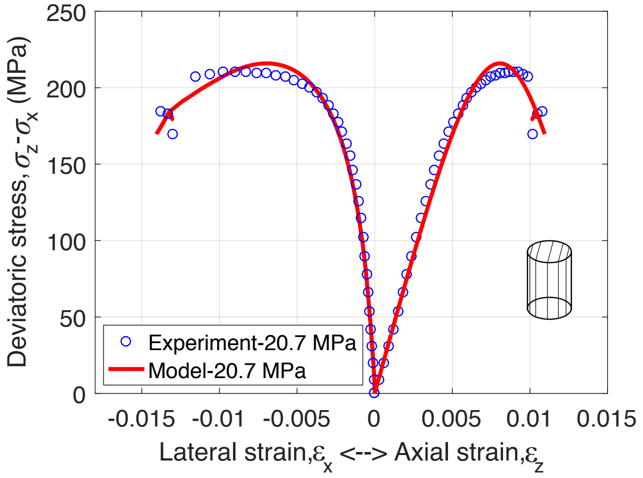

Fig. 3. Calibration of transverse damage parameters.

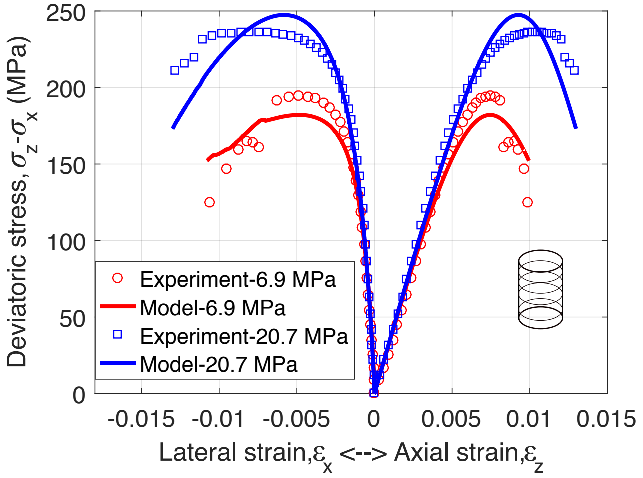

Fig. 4. Calibration of axial damage parameters under different confinements.

Figure 3 shows the experimental stress-strain curve (marker) and the numerical stress-strain curve after calibration (solid line) for an axial loading parallel to the bedding under a confinement of 20.7 MPa. The two curves match closely for deformation both parallel and perpendicular to the loading axis. The proposed model successfully captures the hardening-softening transition. Note that in this simulation, the two lateral strain components were not the same: we averaged them in the figure. Figure 4 shows the experimental stress-strain curve (marker) and the numerical stress-strain curve after calibration (solid line) for an axial loading perpendicular to the bedding plane under confining pressures of 6.9 MPa and 20.7 MPa. The model correctly predicts the increase of compression strength with the increase of confining pressure. Note: the non-smooth part on the prediction curve is due to the discontinuous experimental total strain used for calibration. The calibrated parameters are listed in Table 1. In the absence of stress/strain curves for shear and tension stress paths, some parameters could not be calibrated.

Table 1. Calibrated model parameters

Parameters	Units	Value
E_1	*GPa*	35.9
E_2	*GPa*	37.8
ν_{12}	-	0.224
ν_{23}	-	0.327
ϵ_{11}^{c0}	-	4.239×10^{-4}
β_{11}^{c}	-	1.266×10^{-2}
α_{11}^{c}	-	2.483×10^{-3}
ϵ_{22}^{c0}	-	4.081×10^{-4}
β_{22}^{c}	-	1.131×10^{-2}
α_{22}^{c}	-	1.903×10^{-3}
η	MPa^{-1}	2.077×10^{-4}

2.3. *Single element simulation*

To test whether the proposed anisotropic damage model can predict the variations of compression strength with the orientation of the loading relative to the bedding plane, a series of uniaxial compression test were simulated. A single cubic element was modeled with the calibrated parameters listed in Table 1. We used OOFEM, an open source, object oriented FEM software (**Patzak, 2012**). In the following, angles refer to the angle between the unit vector normal to the bedding plane and the loading axis-x. For simulation with an orientation angle different from 0° and 90°, it is necessary to assume values for parameters G_{12}, ϵ_{12}^{s0}, ϵ_{23}^{s0}, which could not be calibrated from triaxial compression tests. We used: $G_{12} = 14.68GPa$, $\epsilon_{12}^{s0}=2.5\times10^{-4}$, $\epsilon_{23}^{s0}=2.8\times10^{-4}$. Displacements are fixed at one face of the Finite Element. The opposite face is subjected to concentrated forces at the nodes. Stresses and strains are calculated at 8 integration points, and averaged.

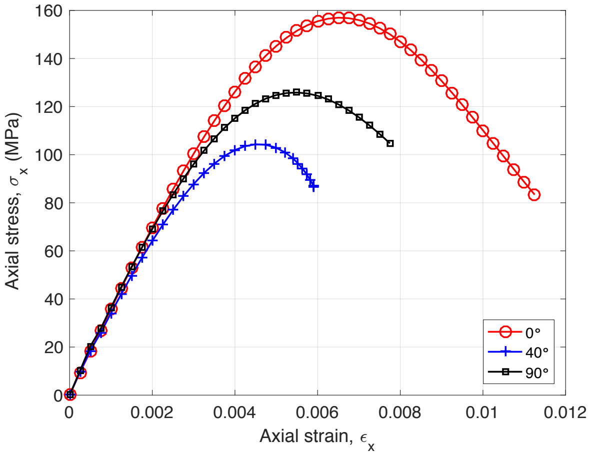

Fig. 5. Simulations of uniaxial compression tests on a single element. Note: the orientation angle represents the angle between the unit vector normal to the bedding plane and the loading axis-x.

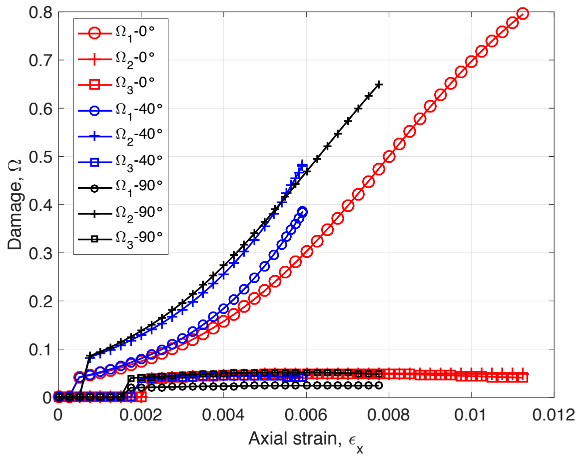

Fig. 6. Evolution of the damage components during the uniaxial compression tests simulated on a single element. Note when the loading axis-x is neither perpendicular to or parallel to the bedding, damage develops in two directions (ω_1, ω_2).

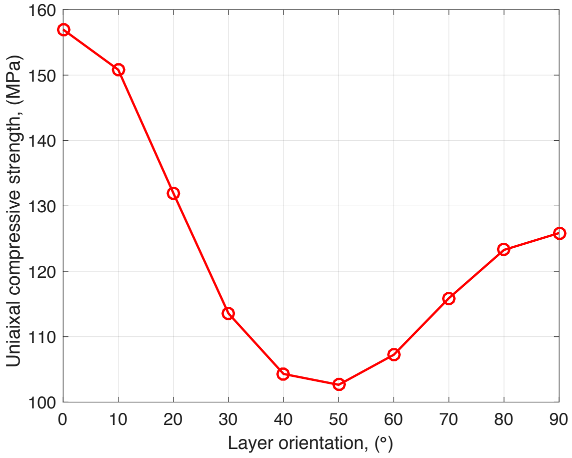

Fig. 7. Variation of uniaxial compressive strength (maximum stress reached during loading) with respect to the orientation of the bedding.

Figure 5 shows the uniaxial compression resulting stress strain curve, which indicates that uniaxial compression strength varies depending on the relative orientation of the bedding plane and the loading axis. The largest compression strength is expected when the sample is loaded in the direction normal to the bedding plane, a smaller value is expected when the loading axis is in the bedding plane; and the smallest value is expected when the sample is loaded with an angle to the bedding plane. The loading direction relative to the bedding does not influence the elastic behavior, because elastic moduli are similar in the axial and transverse directions of the material. Figure 6 shows that damage only develops in direction 1 (perpendicular to the bedding) when the loading orientation is 0°, and gradually changes to direction 2 (parallel to the bedding) as the loading orientation angle increases. Figure 7 provides the variations of uniaxial compressive strength (maximum stress reached during loading) with the loading orientation. Results match existing data for shale (**Niandou et al., 1997**), both in trend and order of magnitude.

Similar to uniaxial compression, uniaxial tension strength depends on the orientation of the loading compared to that of the bedding plane. Damage parameters that could not be calibrated from triaxial compression tests are assigned values commonly found for rock materials (Table 2).

Table 2. Assumed model parameters for tension

Parameters	Units	Value
ϵ_{11}^{t0}	-	1.5×10^{-4}
ϵ_{12}^{s0}	-	1.8×10^{-4}
α_{11}^{t}	-	3.0×10^{-4}
ϵ_{22}^{t0}	-	2.5×10^{-4}
ϵ_{23}^{s0}	-	2.8×10^{-4}
α_{22}^{t}	-	4.0×10^{-4}

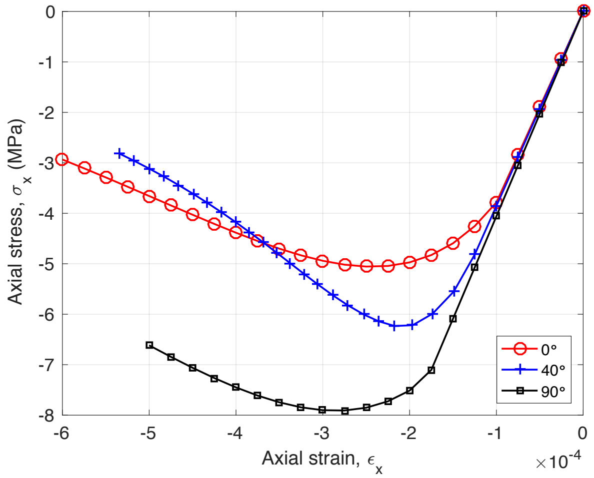

Fig. 8. Simulations of uniaxial tension tests on a single element. Note: the orientation angle represents the angle between the unit vector normal to the bedding plane and the loading axis-x. The soil mechanics sign convention is used.

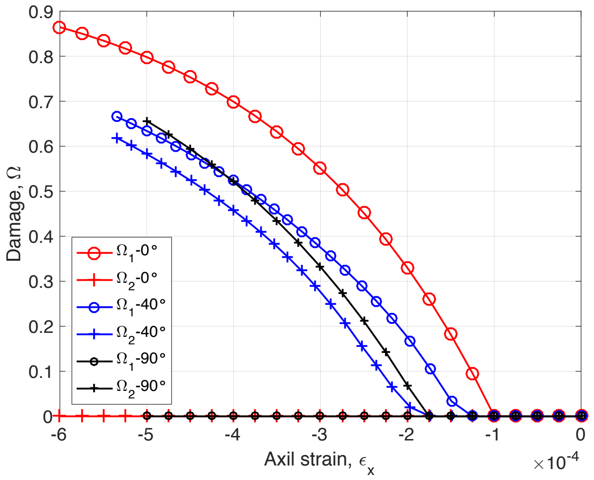

Fig. 9. Evolution of damage components during uniaxial tensile tests simulated on a single element. Damage components change from ω_1 to ω_1, ω_2, and to ω_2 as the orientation angle increases.

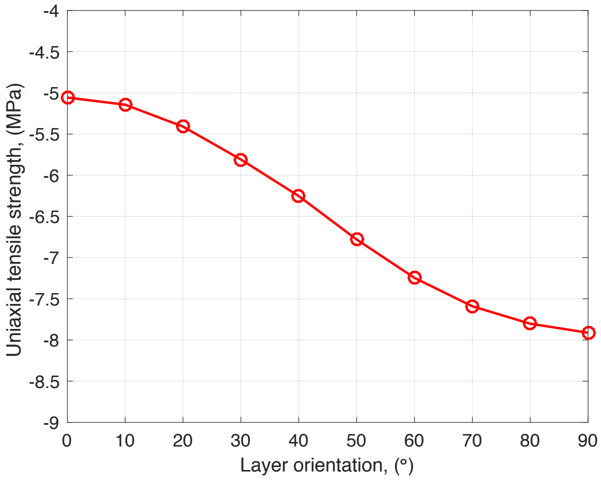

Fig. 10. Variation of uniaxial tensile strength (maximum stress reached during loading) with respect to bedding orientation.

Figure 8 shows the uniaxial tensile stress-stain curves obtained by single element simulation. The tensile strength reaches a maximum for a loading parallel to the bedding, and gradually decreases as the orientation angle decreases. Figure 9 shows the evolution of the damage components during the loading, which all exhibit a rapid increase after the yield point is reached. Similar to the compressive case, only one damage component is non zero when the loading is parallel or perpendicular to the bedding, and two damage components develop when the orientation angle is $\theta = 40°$. Figure 10 provides the variations of uniaxial tensile strength (maximum stress reached during loading) with the loading orientation. Results match existing results of indirect Brazilian tests (**Mohamed et al., 2015**), both in trend and order of magnitude.

3. NONLOCAL IMPLEMENTATION

3.1. Anisotropic nonlocal formulation

Physically, the proposed continuum damage model with strain softening leads to localized deformation. The failure path as well as dissipated energy has no convergent solution upon mesh refinement. Mathematically, the partial differential equation governing quasi-static problems looses ellipticity, which makes the boundary problem ill-posed.

To address these issues, non-local models were proposed (**Pijaudier-Cabot and Bazant, 1987**): the stiffness reduction (damage development) at one material point not only depends on the mechanical state at the point itself, but also relies on the stress-strain value over a certain neighboring domain, characterized by an internal length. Numerically, the internal state variable κ_i, which was used to calculate the damage value, is replaced with a nonlocal state variable κ_i^{nl}. It is calculated from a spatial averaging of equivalent strain over a representative volume V, as follows:

$$\bar{\epsilon}^{eq}(\boldsymbol{x}) = \int_V \alpha_0(\boldsymbol{x}, \boldsymbol{\xi})\, \epsilon^{eq}(\boldsymbol{\xi}) dV(\boldsymbol{\xi}) \tag{15}$$

where $\alpha_0(x, \xi)$ is the chosen nonlocal weight function. For a uniform field, nonlocal variables should be equal to local variables. Thus, the weight functions should satisfy the following normalizing condition in an infinite medium:

$$\int \alpha_0(\boldsymbol{x}, \boldsymbol{\xi}) d\xi = 1 \tag{16}$$

In the vicinity of the boundary of a finite body, it is assumed that the nonlocal operator is only defined on the part that lies within the solid V'. The weight function is normalized through

$$\alpha(x, \xi) = \alpha_0(\boldsymbol{x}, \boldsymbol{\xi}) / \int_{V'} \alpha_0(\boldsymbol{x}, \boldsymbol{\xi}) dV'(\xi). \tag{17}$$

The exact form of weight function depends on the material itself. For an isotropic material, Gaussian distribution functions or bell-shaped functions depending on the distance $\|\boldsymbol{x} - \boldsymbol{\xi}\|$ are simple and powerful tools. Only one coefficient, called internal length, is needed to normalize the weight functions; it represents the material property and is of the same order of magnitude as the maximum size of material heterogeneities. For a transverse isotropic material, the weight function should be direction dependent. As shown the micro-structure in Figure 1, the field variable at a material point should be more influenced by the field variable at points located along the bedding that by the field variable located at same distance perpendicular to the bedding. Figure 11 shows the plots of the weight functions chosen to account for different non-local effects in directions parallel and perpendicular to the bedding.

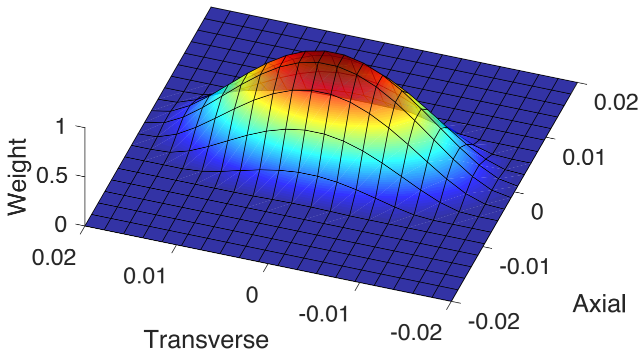

Fig. 11. Weight function chosen in the anisotropic non-local damage model.

The nonlocal influence zone characterized by internal length also represents the fracture process zone size when modelling fracture propagation. Weak bedding planes prevent the process zone to grow when a fracture propagates along the weak bedding. As a result, a smaller process zone is expected compared with the process zone of a fracture propagating perpendicular to the bedding plane. Based on these observations, we redefine the anisotropic bell-shape weight function as

$$\alpha_0(\boldsymbol{x}, \boldsymbol{\xi}) = \langle 1 - \left(\frac{\xi_1 - x_1}{r_1}\right)^2 - \left(\frac{\xi_2 - x_2}{r_2}\right)^2 \rangle^2 \quad . \qquad (18)$$

Where r_1 (respectively, r_2) represents the characteristic internal length within the weak plane (respectively, perpendicular to the bedding), and $r_1 > r_2$. The contour of weight function in Eq. (18) is an ellipse, as shown in Figure 12.

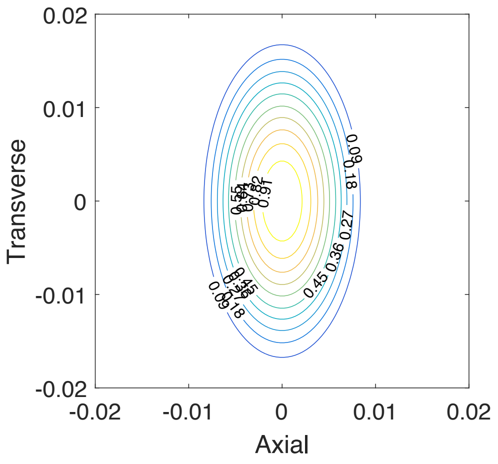

Fig. 12. Contour of the anisotropic bell-shape weight functions.

3.2. *Local arc length control*

Due to the nonlocal contributions from the neighbor points, the element stiffness matrix does not only depend on the state variables calculated at the element node, but also the state variables of other nodes surrounding that element. Ultimately, the half band size of the global stiffness matrix expands. However, this process requires sophisticated mathematical manipulations as shown in **Jirasek and Patzak** (**2002**). It is impossible to obtain an analytical expression for the proposed damage model for cases $0° < \theta < 90°$, as matrix rotation is involved. Instead, the local secant operator was used for computation - at the cost of losing quadratic convergence rate. However, the positive definite global stiffness guarantee global iteration do not stop at early stage.

In our model, the damage evolution is computed in strain space in both local and nonlocal approaches, therefore the implementation of the anisotropic non-local damage model was similar to the implementation of the local model: a local iteration scheme, such as a return mapping algorithm, is not needed to keep the stress state on the yield surface. However, the material softening behavior may induce snap-back and snap through responses at the global force-displacement level. The traditional Newton-Raphson iteration fails to track these types of response both if load control or displacement control is used. To overcome these issues, an Arc length control **(Crisfield, 1981)** was proposed. It essentially adds one macroscopic unknown and one equation, the arc length equation. After solving the N+1 equation system, the displacement and load level can both decrease or increase to keep track of global responses. Spherical arc length control or normal plane control are the two most commonly used techniques. We implement the local version of the normal plane method proposed by **May and Duan (1997)**, in which the relative displacement of nodal points of elements in the fracture process zone (positive damage value) are taken to construct the arc length constraint equation.

4. NUMERICAL SIMULATION OF 3 POINT BENDING

We carried out numerical simulations of a three-point bending test to investigate mode I and mixed mode fracture propagation. The domain is a notched beam under plane strain condition as shown in Figure 13. The normal to the bedding plane is at an angle of 0°, 45°, and 90° with respect to the horizontal x-axis. Figure 13 shows the geometry and symmetrical boundary conditions used in the simulation. We used the material parameters listed in Section 2.3, Table 1 and Table 2.

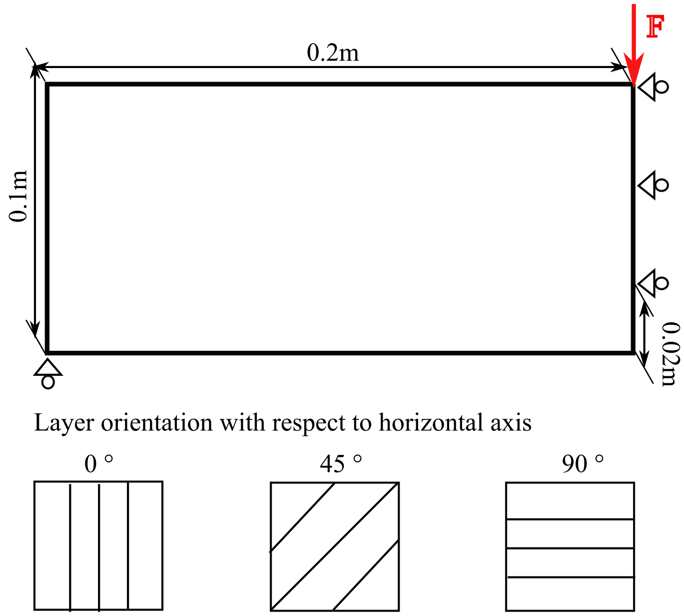

Fig. 13. Geometry and boundary conditions of the simulation domain. Note: the horizontal direction is the x-axis of the domain; the vertical direction is the y-axis of the domain. The local-1 axis is perpendicular to the bedding; the local-2 axis is parallel to the bedding in the material local coordinate system.

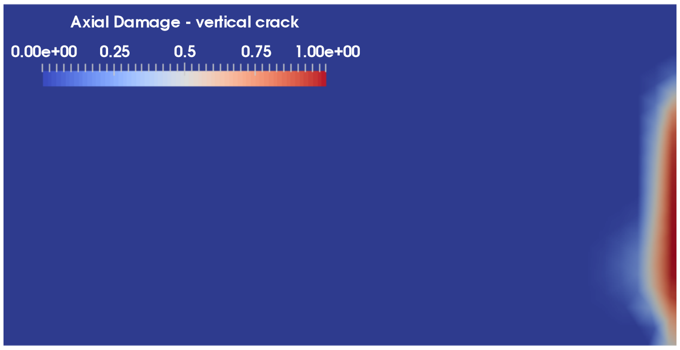

Fig. 14. Local axial damage distribution (vertical cracks) for orientation $\theta = 0°$(vertical bedding) after failure ($F = 0$). Damage propagates in mode I. Note only the coarse mesh results are presented, as there are no significant differences between the two meshes tested.

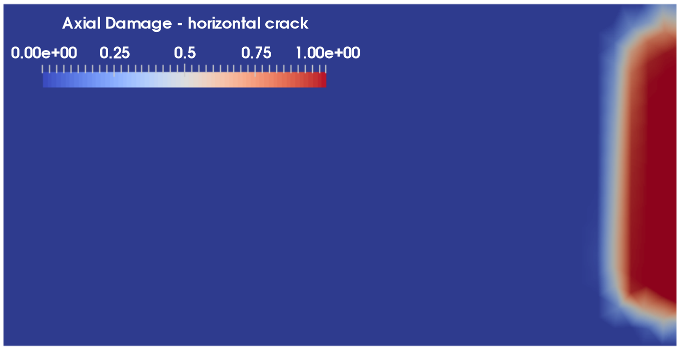

(a)

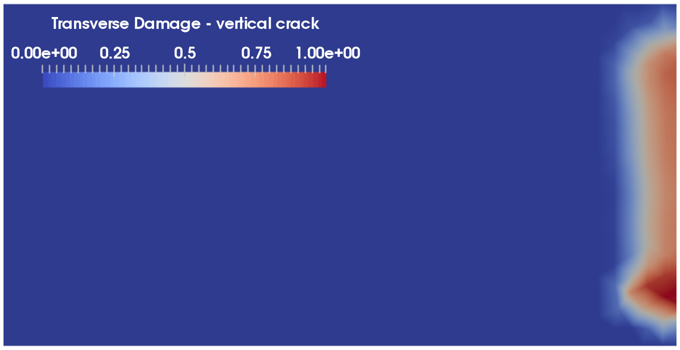

(b)

Fig. 15. (a) Local axial damage (horizontal cracks) distribution, (b) Local transverse damage (vertical cracks) distribution for orientation $\theta = 90°$ (horizontal bedding) after failure ($F = 0$). Damage propagates in mode I (vertical cracks) and II (horizontal cracks due to bedding debonding).

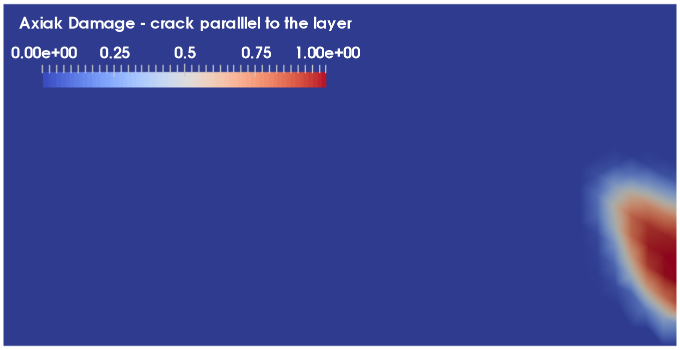

Fig. 16. Local axial damage distribution (crack parallel to the bedding) for $\theta = 45°$. Damage propagates due to the debonding of the bedding. Note this simulation stopped before failure due to numerical convergence issues.

Internal lengths r_1 (parallel to the bedding) and r_2 (perpendicular to the bedding) were 20mm and 10mm, respectively. Two different finite element meshes of three-node triangular elements are used for numerical analysis. No significant difference was noted between the two meshes, which confirms that the non-local model avoids mesh dependence. In the following, only coarse mesh contour results are presented. Figure 14 shows that when the bedding is vertical ($\theta = 0°$), cracks are vertical and the damage process zone lies straight up above the notch. Results agree well with experimental results obtained in isotropic materials: failure is the result of pure mode I fracture propagation. When the bedding is horizontal ($\theta = 90°$), both vertical and horizontal cracks develop within the fracture process zone, as shown in Figure 15. The process zone still spreads vertically above the notch, however, the failure pattern is mostly due to weak bedding debonding as local $\omega_1 > \omega_2$. In addition, compared to the damage distribution for $\theta = 0°$, the size of the process zone is significantly larger due to anisotropic nonlocal effects. These observations conform with physical expectations. Figure 16 shows local axial damage (cracks parallel with weak bedding) for the case $\theta = 45°$. Even through the simulation does not run up to total failure, the failure path is still clear: the damage process zone is oriented perpendicular to the bedding instead of spreading out vertically.

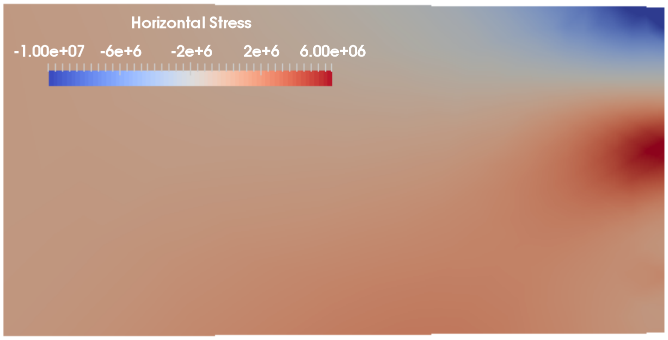

(a) Horizontal stress for $\theta = 0°$

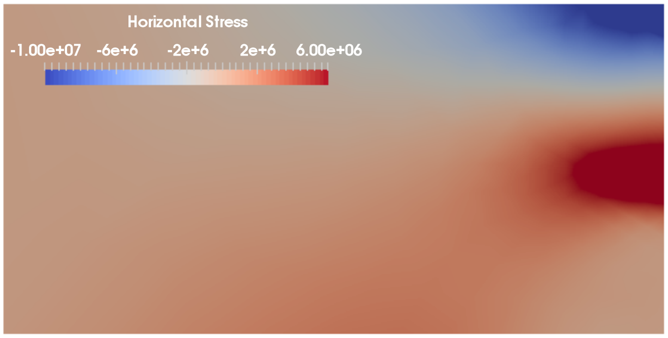

(b) Horizontal stress for $\theta = 45°$

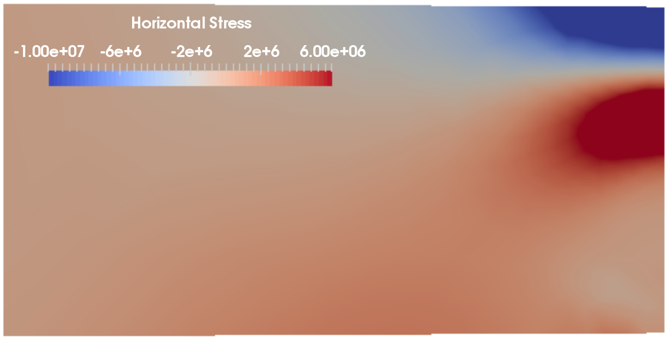

(c) Horizontal stress for $\theta = 90°$

Fig. 17. Horizontal stress distribution after fracture initiates.

Figure 17 shows the horizontal stress distribution for the three cases under study ($\theta = 0°, 45°, 90°$). Intrinsic anisotropy has a significant influence not only on the damage process zone and the failure mechanism (as illustrated in Figure 14-16), but also on the distribution, magnitude and concentrations of stresses. Figure 18 shows the force/displacement curve obtained by numerically at the point where the load is applied. No mesh dependency is noted, which confirms the efficiency of non-local enrichment. The orientation of the loading relative to the bedding dictates the global response: for $\theta = 0°$ the response is more brittle than for $\theta = 90°$, i.e. less energy is needed to fracture the material at $\theta = 90°$. Note for the case of $\theta = 0°$, the snap back behavior (decreasing load with decreasing displacement) is successfully captured thanks to the arc length control method applied locally.

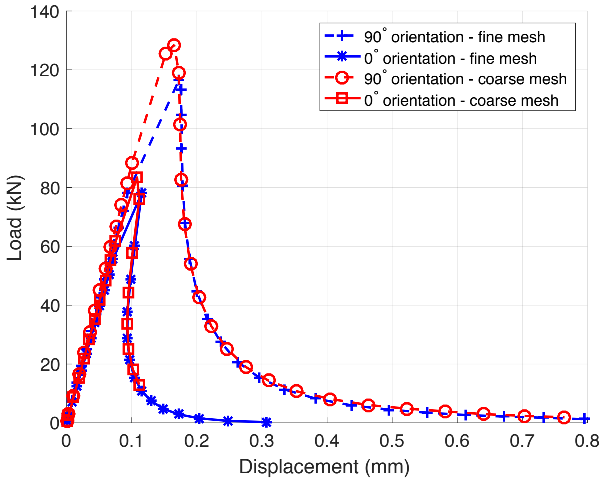

Fig. 18. Load-deflection curve of the simulated cases of $\theta = 90°, 0°$ for different mesh.

5. CONCLUSION

A phenomenological nonlocal anisotropic damage model is formulated for transverse isotropic brittle materials such as sedimentary rocks. Based on the Hashin's failure criteria for unidirectional fiber composites, equivalent strains are defined for tension and compression, within the bedding plane and perpendicular to the bedding plane. Damage propagates when equivalent strains exceed a damage variable that plays the role of an internal variable. Constitutive equations are proposed to relate explicitly this internal variable to the damage variable used in the expression of stiffness. The model is calibrated against triaxial compression test data, for different confinement and loading orientations. Utilizing the calibrated parameters along with some assumed parameters characterizing tensile damage evolution, we simulated uniaxial compression and uniaxial tension tests using a single cubic finite element. The variations of uniaxial tensile and compressive strengths with the orientation of the loading relative to the bedding follow the trends and magnitudes noted in experiments. Anisotropic non-local equivalent strains were used in the formulation to avoid localization and mesh dependence encountered with strain softening. Two different internal length parameters are used to distinguish the non-local effects along and perpendicular to the bedding. An arc length control algorithm is used at the global displacement-force iteration level to avoid convergence issues encountered in the non-local formulation. We simulated several cases of three-point bending tests in plane strain. The nonlocal approach indeed eliminates mesh dependency. Results show that the orientation and size of the damage process zone are direction dependent, and that materials with intrinsic transverse isotropy exhibit mixed fracture propagation modes except when the bedding aligns with the loading direction. Further research towards a multiscale hydro-mechanical fracture propagation scheme is undergoing (**Jin et al., 2017**), in damaged elements are replaced by a discrete portion of fracture modeled with the XFEM, which will allow simulating hydraulic fracturing in rocks exhibiting porosity at multiple scales.

ACKOWLEGEMENTS

Funding to perform this research was provided by the U.S. National Science Foundation (CAREER grant CMMI 1552368).

REFERENCES

1. Donath, F.A., 1961. Experimental study of shear failure in anisotropic rocks. *Geological Society of America Bulletin*. 72(6): 985-989.
2. Niandou, H., J. F. Shao, J. P. Henry and D. Fourmaintraux, 1997. Laboratory investigation of the mechanical behavior of Tournemire shale. *International Journal of Rock Mechanics and Mining Sciences.* 34(1): 3-16.
3. Pietruszczak, S., and Z. Mroz., 2001. On failure criteria for anisotropic cohesive frictional materials. *International Journal for Numerical and Analytical Methods in Geomechanics*. 25(5): 509-524.
4. Mahjoub, M., A. Rouabhi, M. Tijani, and S. Granet, 2015. A damage model for transversely isotropic materials. *In Petrus PhD Conference.*
5. Pietruszczak, S., D. Lydzba and J. F. Shao, 2002. Modelling of inherent anisotropy in sedimentary rocks. *International Journal of Solids and Structures.* 39(3): 637-648.
6. Chen, L., J. F. Shao, Q. Z. Zhu, and G. Duveau, 2012. Induced anisotropic damage and plasticity in initially anisotropic sedimentary rocks. *International Journal of Rock Mechanics and Mining Sciences*. 51:13-23.
7. Bramlette, M. N., 1943. U.S. Geological Survey Professional paper 212, Plate 15-B.
8. Huerta, A. and G. Pijaudier-Cabot, 1994. Discretization influence on regularization by two localization limiters. *Journal of Engineering Mechanics*. 120(6): 1198-1218.
9. Mazars, J., 1986. A description of micro-and macroscale damage of concrete structures. *Engineering Fracture Mechanics* 25(5): 729-737.
10. De Vree, J. H. P., W. A. M. Brekelmans, and M. A. J. Van Gils, 1995. Comparison of nonlocal approaches in continuum damage mechanics. *Computers & Structures*. 55(4): 581-588.
11. Hashin, Z., 1980. Failure criteria for unidirectional fiber composites. *Journal of Applied Mechanics*. 47(2): 329-334.
12. Hill, R., 1948. A theory of the yielding and plastic flow of anisotropic metals. *In Proceedings of the Royal Society of London A: Mathematical, Physical and Engineering Sciences.* 193(1033): 281-297. The Royal Society.
13. Amendt D., S. Busetti and Q. Wenning, 2013. Mechanical characterization in unconventional reservoirs: a facies-based methodology. *Petrophysics* 54(05):457–464.
14. Patzák, B., 2012. OOFEM-an object-oriented simulation tool for advanced modeling of materials and structures. *Acta Polytechnica*. 52(6).
15. Pijaudier-Cabot, G., and Bazant, Z. P., 1987. Nonlocal damage theory. *Journal of Engineering Mechanics*. 113(10), 1512-1533.
16. Jirásek, M., and B. Patzák, 2002. Consistent tangent stiffness for nonlocal damage models. *Computers & Structures* 80(14): 1279-1293.
17. Crisfield, M. A., 1981. A fast incremental/iterative solution procedure that handles “snap-through". *Computers & Structures.* 13(1-3): 55-62.
18. May, I. M., and Y. Duan, 1997. A local arc-length procedure for strain softening. *Computers & Structures*. 64(1): 297-303.
19. Jin, W., H. Xu, C. Arson and S. Busetti, 2017. Computational model coupling mode II discrete fracture propagation with continuum damage zone evolution. *International Journal for Numerical and Analytical Methods in Geomechanics*. 41(2): 223-250.